

# Estimating the coherence of noise in quantum control of a solid-state qubit

Guanru Feng,<sup>1,2</sup> Joel J. Wallman,<sup>1,3</sup> Brandon Buonacorsi,<sup>1,2</sup> Franklin H. Cho,<sup>1,2</sup> Daniel K. Park,<sup>1,2,4</sup> Tao Xin,<sup>1,2,5</sup> Dawei Lu,<sup>1,2</sup> Jonathan Baugh,<sup>1,2,6,\*</sup> and Raymond Laflamme<sup>1,2,7,8,†</sup>

<sup>1</sup>*Institute for Quantum Computing, Waterloo, Ontario, N2L 3G1, Canada*

<sup>2</sup>*Department of Physics and Astronomy, University of Waterloo, Waterloo, Ontario, N2L 3G1, Canada*

<sup>3</sup>*Department of Applied Mathematics, University of Waterloo, Waterloo, Ontario, N2L 3G1, Canada*

<sup>4</sup>*Natural Science Research Institute, Korea Advanced Institute of Science and Technology, Daejeon, 34141, South Korea*

<sup>5</sup>*Department of Physics, Tsinghua University, Beijing 100084, China*

<sup>6</sup>*Department of Chemistry, University of Waterloo, Waterloo, Ontario, N2L 3G1, Canada*

<sup>7</sup>*Perimeter Institute for Theoretical Physics, Waterloo, Ontario, N2J 2W9, Canada*

<sup>8</sup>*Canadian Institute for Advanced Research, Toronto, Ontario M5G 1Z8, Canada*

(Dated: December 9, 2016)

To exploit a given physical system for quantum information processing, it is critical to understand the different types of noise affecting quantum control. Distinguishing coherent and incoherent errors is extremely useful as they can be reduced in different ways. Coherent errors are generally easier to reduce at the hardware level, e.g. by improving calibration, whereas some sources of incoherent errors, e.g.  $T_2^*$  processes, can be reduced by engineering robust pulses. In this work, we illustrate how purity benchmarking and randomized benchmarking can be used together to distinguish between coherent and incoherent errors and to quantify the reduction in both of them due to using optimal control pulses and accounting for the transfer function in an electron spin resonance system. We also prove that purity benchmarking provides bounds on the optimal fidelity and diamond norm that can be achieved by correcting the coherent errors through improving calibration.

A key obstacle to realizing scalable quantum information processing (QIP) is implementing quantum gates sufficiently precisely so that errors can be detected and corrected [1–6]. This requires both the intrinsic noise and the noise in the control to be characterized. The combined noise can be completely characterized using either quantum process tomography (QPT) [7, 8] or gate set tomography (GST) [9, 10]. However, these methods are time-consuming and scale exponentially in the number of qubits.

Instead of completely characterizing a system, we can efficiently quantify how noisy the experimental operations are. The most prominent method along these lines is randomized benchmarking (RB) [12–17], which gives an efficient estimate of the benchmarking error per gate (BEPG) defined as

$$\epsilon(\mathcal{E}) = 1 - F = 1 - \int d\psi \langle \psi | \mathcal{E}(|\psi\rangle\langle\psi|) | \psi \rangle, \quad (1)$$

where  $\mathcal{E}$  is the noise channel and the integral (the channel fidelity  $F$ ) is over all pure states  $|\psi\rangle$  according to the Haar measure. However, the BEPG is, by construction, insensitive to many of the particular details of the noise mechanism. As errors due to different noise mechanisms can be corrected in different ways and have different impacts on QIP, understanding the noise characteristics in quantum systems is of critical importance.

Noise characteristics can be broadly grouped as either coherent (unitary) or incoherent (statistical). Coherent noise is usually due to systematic control errors in, for example, imperfect rotation angles or axes [18, 19], which may be easier to reduce than incoherent noise such as  $T_1$  and  $T_2$  processes. The BEPG for coherent noise accumulates quadratically with the number of gates whereas incoherent noise accumulates linearly. Furthermore, coherent and incoherent noises with the same BEPG may lead to dramatically different thresholds

as quantified by the worst-case error per gate (WEPG), also known as the diamond distance, [20]

$$\epsilon_\diamond = \frac{1}{2} \max_{\psi} \|[\mathcal{E} - \mathcal{I}] \otimes \mathcal{I}(\psi)\|_1, \quad (2)$$

where  $\|A\|_1 = \text{Tr} \sqrt{A^\dagger A}$  and  $\mathcal{I}$  is the identity channel acting on an ancillary system of the same size to account for the effect of the noise on entangled inputs. Therefore, identifying whether the noise is primarily coherent or incoherent is essential for determining an appropriate error threshold when evaluating a physical system and for determining whether experimental effort should prioritize improving calibration or suppressing incoherent error processes.

Several approaches have been developed to provide more information about the noise than just the BEPG while retaining the advantages of RB [21–24]. In particular, purity benchmarking (PB) [23] enables the quantification of the coherence of a noise process without assuming a specific noise model, which can be used to obtain an improved estimate of the WEPG [25, 26], whereas the method of Ref. [24] detects additive coherent errors under specific assumptions about the noise model.

In this paper, we show that PB can be used to quantify the best achievable BEPG and WEPG under optimal control for single-qubit systems. We then test PB in a specific modality, namely, a solid-state electron spin resonance (ESR) system. Bulk ESR samples consist of an ensemble of (nearly) identical spins, which can mimic the behaviour of a fixed number of qubits depending on the structure of the solid and the species of the spins. ESR provides one path to scalable QIP using techniques such as algorithmic cooling and distributed node quantum information processing [27], which are viable because electron spins have larger thermal polarization and faster relaxation rates than nuclear spins, and hyperfine-

coupled nuclear spins can also be efficiently controlled using ESR techniques [28–30]. The quantum control techniques developed in QIP are also very useful for modern ESR spectroscopy [31, 32]. Achieving high fidelity quantum control in ESR is challenging due to the limited bandwidth of a conventional microwave resonator. In this work, RB and PB protocols are used to assess the control accuracy of an ensemble single-qubit system. We demonstrate the reduction in both the coherent and incoherent errors obtained by first using the transfer function of the microwave control system to correct numerically-derived optimal control (OC) pulses [33] and then using a spin-packet selection technique to effectively reduce the inhomogeneous spectral broadening [34]. The lowest values we obtained for BEPG ( $\epsilon$ ) and the incoherent error ( $\epsilon_{\text{in}}$ , defined below) for Clifford gates are  $6.3 \times 10^{-3}$  and  $5.4 \times 10^{-3}$ , respectively.

*The incoherent error per gate*—The primary characteristic of a coherent noise process is that it can be corrected by directly reversing the unitary process with perfect control. We therefore define the incoherent error per gate (IEPG) of a noise channel  $\mathcal{E}$  to be the optimal BEPG that can be achieved by correcting  $\mathcal{E}$  with perfect unitary operations, that is,

$$\epsilon_{\text{in}}(\mathcal{E}) = \min_{\mathcal{U}, \mathcal{V}} \epsilon(\mathcal{U} \circ \mathcal{E} \circ \mathcal{V}) \quad (3)$$

for any unitary operations  $\mathcal{U}$  and  $\mathcal{V}$ . For a general  $d$ -dimensional system, the incoherent error satisfies

$$\epsilon(\mathcal{E}) \geq \epsilon_{\text{in}}(\mathcal{E}) \geq \frac{d-1}{d} \left[ 1 - \sqrt{u(\mathcal{E})} \right], \quad (4)$$

where the unitarity is [23]

$$u(\mathcal{E}) = \frac{d}{d-1} \int d\psi \text{Tr}[\mathcal{E}(|\psi\rangle\langle\psi| - \frac{1}{d}\mathbb{1}_d)]^2. \quad (5)$$

We now show that the lower bound on the incoherent error in Eq. (4) is saturated to  $O[\epsilon_{\text{in}}(\mathcal{E})^2]$  in the single-qubit case. Let  $\mathcal{E}_{j,k} = \text{Tr}[\sigma_j^\dagger \mathcal{E}(\sigma_k)]/2$  be the process matrix of  $\mathcal{E}$ , where  $\{\sigma_0, \sigma_1, \sigma_2, \sigma_3\} = \{\mathbb{1}_2, \sigma_x, \sigma_y, \sigma_z\}$ . The process matrix of any completely-positive and trace-preserving (CPTP) noise channel can be written in block form as

$$\mathcal{E} = \begin{pmatrix} 1 & \mathbf{0} \\ \mathcal{E}_n & \mathcal{E}_u \end{pmatrix}. \quad (6)$$

The unitarity and BEPG of  $\mathcal{E}$  are

$$\begin{aligned} u(\mathcal{E}) &= \frac{1}{3} \text{Tr} \mathcal{E}_u^\dagger \mathcal{E}_u \\ \epsilon(\mathcal{E}) &= \frac{1}{6} \text{Tr} (\mathbb{1}_3 - \mathcal{E}_u). \end{aligned} \quad (7)$$

Any single-qubit noise channel can be corrected to another channel  $\mathcal{E}'$  such that  $\mathcal{E}'_u = \Sigma$  and  $\mathcal{E}'_n = (0, 0, \lambda)^T$  for some  $\lambda$  and some real diagonal  $\Sigma$  by applying suitable (perfect) unitary operators [35], which leaves the unitarity unchanged, that

is,  $u(\mathcal{E}) = u(\mathcal{E}') = \text{Tr} \Sigma^2$ . By Von Neumann's trace inequality,

$$\epsilon(\mathcal{E}') \leq \epsilon(\mathcal{U} \circ \mathcal{E} \circ \mathcal{V}) \quad (8)$$

for any unitary operations  $\mathcal{U}$  and  $\mathcal{V}$ , so  $\epsilon(\mathcal{E}') = \epsilon_{\text{in}}(\mathcal{E})$ . Writing  $\Sigma = \mathbb{1}_3 - \epsilon(\mathcal{E}')\delta$  where  $\delta$  is nonnegative for any CPTP map [36] and  $\text{Tr} \delta = 6$  from Eq. (7), we have

$$\begin{aligned} u(\mathcal{E}) &= 1 - \frac{2\epsilon(\mathcal{E}')}{3} \text{Tr} \delta + \frac{\epsilon(\mathcal{E}')^2}{3} \text{Tr} \delta^2 \\ &= 1 - 4\epsilon(\mathcal{E}') + (4+c)\epsilon(\mathcal{E}')^2, \end{aligned} \quad (9)$$

for a single qubit. The minimum and maximum values of  $c$  subject to  $\epsilon(\mathcal{E}') \leq 1/3$ ,  $\text{Tr} \delta = 6$ , and the CPTP constraints [17, 36] are 0 and 2, attained when  $\delta = 2\mathbb{1}_3$  and  $\delta_{1,1} = \delta_{2,2} = 3$  respectively. Therefore the incoherent error for a single qubit satisfies

$$\epsilon_{\text{in}}(\mathcal{E}) = \epsilon(\mathcal{E}') = \frac{1}{2} \left( 1 - \sqrt{u(\mathcal{E})} \right), \quad (10)$$

to within  $\epsilon_{\text{in}}(\mathcal{E})^2/2$  as claimed.

Now we consider the part of error that is removed by the optimal unitary corrections. With  $\mathcal{E} = \mathcal{U} \circ \mathcal{E}' \circ \mathcal{V}$  and  $\mathcal{W} = \mathcal{V} \circ \mathcal{U}$ , from Eq. (7) the BEPG of  $\mathcal{E}$  is

$$\begin{aligned} \epsilon(\mathcal{E}) &= \frac{1}{6} \text{Tr}(\mathbb{1}_3 - \Sigma) + \frac{1}{6} \text{Tr}(\mathbb{1}_3 - \mathcal{W}_u) \\ &\quad - \frac{1}{6} \text{Tr}(\mathbb{1}_3 - \mathcal{W}_u)(\mathbb{1}_3 - \Sigma) \\ &= \epsilon_{\text{in}}(\mathcal{E}) + \epsilon(\mathcal{W}) + O[\epsilon_{\text{in}}(\mathcal{E})\epsilon(\mathcal{W})] \end{aligned} \quad (11)$$

where the order of the higher-order term comes from  $\Sigma$  being diagonal and the diagonal elements of a generic CPTP map  $\mathcal{M}$  being  $1 - O(\epsilon(\mathcal{M}))$  [17]. We can regard  $\mathcal{U}$  and  $\mathcal{V}$  as coherent errors and so the BEPG of the (composite) coherent error is

$$\epsilon_{\text{coh}}(\mathcal{E}) = \epsilon(\mathcal{W}) = \epsilon(\mathcal{E}) - \epsilon_{\text{in}}(\mathcal{E}) + O(\epsilon_{\text{in}}(\mathcal{E})\epsilon(\mathcal{W})), \quad (12)$$

which is also equivalent [to  $O(\epsilon_{\text{in}}(\mathcal{E})\epsilon(\mathcal{W}))$ ] to the BEPG removed by the optimal unitary corrections.

The IEPG also provides an improved bound on the optimal WEPG  $\epsilon_{\circ, \text{opt}}$  that can be achieved by applying unitary corrections. Let  $\mathcal{E}'_u$  be the unital part of  $\mathcal{E}'$ , that is, the channel such that  $\mathcal{E}'(A) = \mathcal{E}'_u(A) + \lambda\sigma_z \text{Tr} A$  for all  $A \in \mathbb{C}^{2 \times 2}$ . We then have

$$\mathcal{E}' \otimes \mathcal{I}(\rho) = \mathcal{E}'_u \otimes \mathcal{I}(\rho) + \lambda\sigma_z \otimes \text{Tr}_1 \rho \quad (13)$$

where  $\text{Tr}_1 \rho$  is the partial trace over the first system. By the triangle inequality and submultiplicativity of the diamond norm,

$$\begin{aligned} \epsilon_{\circ}(\mathcal{E}') &\leq \epsilon_{\circ}(\mathcal{E}'_u) + |\lambda| \max_{\psi} \|\text{Tr}_1 \psi\|_1 \\ &\leq \epsilon_{\circ}(\mathcal{E}'_u) + \sqrt{2}|\lambda|, \end{aligned} \quad (14)$$

where the maximization is achieved by any maximally entangled state. As  $\mathcal{E}'_u$  is a Pauli channel [11, 16],  $|\lambda| \leq 3\epsilon(\mathcal{E}')$  and

with a lower bound on the WEPG in terms of the BEPG [17], we have

$$\epsilon_{\circ, \text{opt}}(\mathcal{E}) = \epsilon_{\circ}(\mathcal{E}') \in [\frac{3}{2}\epsilon_{\text{in}}(\mathcal{E}), (\frac{3}{2} + 3\sqrt{2})\epsilon_{\text{in}}(\mathcal{E})]. \quad (15)$$

Both these constraints are linear in  $\epsilon_{\text{in}}(\mathcal{E})$  and so give reasonable estimates as  $\epsilon_{\text{in}}(\mathcal{E})$  decreases compared to the gap between the optimal scalings for the lower and upper bounds in terms of  $\epsilon(\mathcal{E})$  alone, which diverge by orders of magnitude as  $\epsilon(\mathcal{E})$  decreases [20].

*Experimental Implementation*—Our X-band pulsed ESR spectrometer was custom-built for QIP experiments and includes arbitrary waveform generation and a loop-gap resonator for sub-millimeter sized samples that allows for relatively broadband control [34]. For an ensemble single-qubit system, we use a sample of gamma-irradiated fused quartz, a paramagnetic sample in powder form where the primary defect is a spin-1/2 unpaired electron at an oxygen vacancy [37], with  $T_1 \sim 160 \mu\text{s}$ ,  $T_2 \sim 30 \mu\text{s}$ , and  $T_2^* \sim 80 \text{ ns}$ .

A pulse generated with an initial waveform  $W(f)$  in the frequency-domain representation will be distorted to a new waveform  $W'(f)$  seen by the spins due to the system's transfer function  $\mathcal{T}$ , which is the frequency-domain representation of the impulse response of the system [38, 39], so that  $W' = \mathcal{T} \cdot W$  where  $\cdot$  denotes the point-wise product of  $\mathcal{T}$  and  $W$ . The transfer function includes contributions from the resonator's transfer function and other imperfections in the pulse generation and transmission. One method to correct  $W'(f)$  is to distort the initial waveform to be  $\mathcal{T}^{-1} \cdot W$ . The accuracy of this method is limited by the accuracy with which  $\mathcal{T}$  can be determined. We measure  $\mathcal{T}$  by detecting Rabi oscillations of the electron spins as a function of the microwave frequency [40]. This measured transfer function, denoted by  $\mathcal{T}_{\text{meas}}$ , is then used to modify the input OC pulse so that the distorted pulse seen by the spins will approximate the desired waveform.

We use three OC pulses:  $\pi/2$  and  $\pi$  rotations (denoted by X90, X180, Y90 and Y180 for rotations around the  $x$ - and  $y$ -axes respectively) and an identity operation (denoted by  $\mathcal{I}$ ). The pulses are each 150 ns long and designed to be robust to distributions of Larmor frequency and microwave ( $B_1$ ) field that closely mimic the measured properties of the combined system of our sample and resonator [40]. The design fidelity of each pulse exceeds 99.7% when averaged over these distributions [40]. The experimental results span three different conditions for implementing the OC pulses: (1) not taking the system transfer function into account, *i.e.*, assuming  $\mathcal{T} = 1$  for all frequencies, (2) modifying the input pulses using  $\mathcal{T}_{\text{meas}}$ , and (3) the same as (2) but also implementing a spin-packet selection (SEL) state preparation sequence [34] which effectively increases  $T_2^*$  by a factor of 2.

We implement the 24 elements of the Clifford group as  $\mathbf{G} = \mathcal{S}\mathcal{P}\mathcal{Z}$  where  $\mathcal{S} \in \{\mathcal{I}, \text{X90}, \text{Y90}\}$ ,  $\mathcal{P} \in \{\mathcal{I}, \text{Y180}\}$ , and  $\mathcal{Z} \in \{\mathcal{I}, \text{Z90}, \text{Z180}, \text{Z270}\}$ .  $\mathcal{S}$  and  $\mathcal{P}$  are implemented using the numerically derived  $\mathcal{I}$ ,  $\pi/2$  and  $\pi$  pulses and altering the phase as needed to achieve  $x$ - and  $y$ -axis rotations. The operations in  $\mathcal{Z}$  are implemented virtually by changing

the reference frame [42]. The initial state in all experiments is represented by the deviation density matrix  $\sigma_z$ .

We can estimate the BEPG and IEPG averaged over the set of operations  $\mathbf{G}$  via RB and PB as follows [15, 23] (see the quantum circuits in Fig. 1). (1) Prepare the state  $\sigma_z$ . (2) Apply a sequence of  $m$  uniformly-random operations from  $\mathbf{G}$ , which maps  $\sigma_z$  to  $\rho_j$ . (2.1) For RB, apply a recovery gate  $R \in \mathbf{G}$  that maps  $\rho_j$  back to  $\pm\sigma_z$ . When the final state is  $-\sigma_z$  we change the sign to be positive in post-processing, that is, implement a virtual X gate. (3) For RB, estimate the expectation value  $\langle\sigma_z\rangle$ . For PB, estimate the purity

$$P = \langle\sigma_x\rangle^2 + \langle\sigma_y\rangle^2 + \langle\sigma_z\rangle^2 \quad (16)$$

of the final state  $\rho_j$ . Averaging over random sequences of length  $m$  and fitting to

$$\begin{aligned} \langle\sigma_z\rangle &= A_z + B(1 - 2\epsilon)^m \\ \langle P \rangle &= A' + B'u^{m-1} \end{aligned} \quad (17)$$

for RB and PB, respectively, under trace-preserving noise, allows  $\epsilon$  and the unitarity  $u$  (and hence  $\epsilon_{\text{in}}$  via Eq. (10)) to be estimated where the constants absorb the state preparation and measurement (SPAM) errors and the non-unitality of the noise. In particular,  $A' = \sum_M A_M^2$  ( $M \in \{\sigma_x, \sigma_y, \sigma_z\}$ ) with

$$A_M = \text{Tr } M\mathcal{E}(\frac{1}{2}\mathbb{1}_2) = \frac{1}{24} \sum_G \text{Tr } M\mathcal{E}(G\rho G^\dagger), \quad (18)$$

where the summation is over the single-qubit Clifford group and the equality follows from the fact that the Clifford group is a unitary 2-design and hence is also a unitary 1-design [14]. We can therefore estimate both constant off-sets by performing a single Clifford gate, measuring the expectation values of  $\langle\sigma_z\rangle$ ,  $\langle\sigma_x\rangle$ , and  $\langle\sigma_y\rangle$  and averaging over all Clifford gates. The expectation values are measured by the corresponding spin echo detection sequences in Figs. 1(c) and (d). We sample 150 random sequences for each sequence length  $m$  of RB and PB independently.

*Results and Discussion*—The results of the RB and PB experiments are presented in Fig. 2, with the corresponding estimates for the BEPG, IEPG, coherent error rate and optimal WEPG listed in Table IV.

Pulse distortion due to the system transfer function is significant, as the transfer function bandwidth of  $\sim 100$  MHz is comparable to the pulse excitation bandwidth. The improvement between results from the unmodified OC pulses ( $\mathcal{T} = 1$ ) and those modified by taking into account  $\mathcal{T}_{\text{meas}}$  in Table IV demonstrates substantial reduction in  $\epsilon_{\text{coh}}$  from  $\sim 10^{-2}$  to  $\sim 10^{-3}$ . The  $\epsilon_{\text{in}}$  is also reduced by approximately a factor of two, from  $\sim 1.0 \times 10^{-2}$  to  $\sim 0.5 \times 10^{-2}$ . This shows that the pulse distortion is non-negligible, and causes both coherent and incoherent errors. The larger incoherent error for the unmodified OC pulses is largely due to the OC pulses losing their engineered robustness to Larmor frequency and  $B_1$  inhomogeneities when assuming  $\mathcal{T} = 1$ .

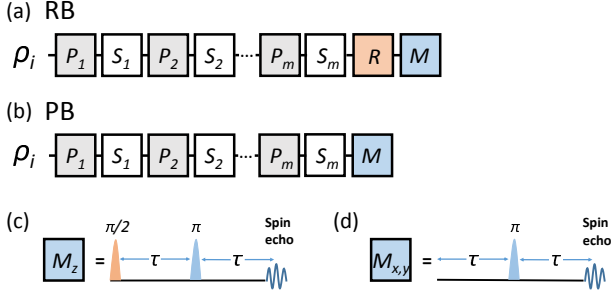


Figure 1. (Color online) Quantum circuits for (a) RB and (b) PB. The initial state  $\rho_i$  is  $\sigma_z$  and the measurements  $M$  are spin echo detection sequences for measuring  $\langle \sigma_z \rangle$  for RB and  $\langle \sigma_{x,y,z} \rangle$  for PB.  $R$  in (a) is the recovery gate that returns the state to  $\pm \sigma_z$ . A total of 150 random sequences with  $S_j \in \{\mathcal{I}, X90, Y90\}$  and  $P_j \in \{\mathcal{I}, X180\}$  (and virtual  $z$ -axis rotations) are applied for each sequence length  $m$  for RB and PB. (c) and (d) are the spin echo detection sequences for measuring  $\langle \sigma_z \rangle$  and  $\langle \sigma_{x,y} \rangle$ , respectively. The  $\pi/2$  and  $\pi$  pulses are 35 ns Gaussian pulses around the  $y$ -axis, and  $\tau=700$  ns represents a delay.

	$\mathcal{T} = 1$	$\mathcal{T} = \mathcal{T}_{\text{meas}}$	$\mathcal{T} = \mathcal{T}_{\text{meas}}$
	no SEL	no SEL	SEL
$\epsilon$	0.0234(11)	0.0073(2)	0.0063(2)
$\epsilon_{\text{in}}$	0.0105(10)	0.0066(2)	0.0054(2)
$\epsilon_{\text{coh}}$	0.0129(21)	0.0007(4)	0.0009(4)
$\epsilon_{\diamond, \text{opt}}$	0.040(26)	0.024(15)	0.020(12)

Table I. Estimates of the BEPG  $\epsilon$ , IEPG  $\epsilon_{\text{in}}$ , coherent error rate  $\epsilon_{\text{coh}}$  and optimal WEPG under perfect calibration  $\epsilon_{\diamond, \text{opt}}$  per Clifford gate. Gates are realized with OC pulses that assume a flat transfer function ( $\mathcal{T} = 1$ ) or are distorted based on the measured transfer function ( $\mathcal{T} = \mathcal{T}_{\text{meas}}$ ), and with or without spin packet selection (SEL) sequences respectively. Note that the values listed here are obtained by fitting the RB and PB data to a single-exponential decay, whereas the actual decays are non-exponential, especially noticeable in the  $\mathcal{T} = 1$  case. Thus, the estimated gate errors given here are effectively averaged over the non-Markovian noise (see main text).

Although the decay rates of both the RB and PB experimental results are substantially reduced by using  $\mathcal{T}_{\text{meas}}$  to improve the OC pulses, the decays seem to deviate from a single exponential decay (i.e., see the oscillating deviations of the orange data points from the orange solid lines in Fig. 2), implying the existence of non-Markovian noise. In our system, the Larmor frequency distribution for different spin-packets ( $T_2^*$  effect) results in a significant non-Markovian effect [34, 43]. The benchmarking pulse sequences act like filters, in that the spectral line-width of the part of the spin-packet that contributes to the signal decreases with the number of gates. This means the effective  $T_2^*$  lifetime is not constant but increases with the number of gates that are implemented. Therefore, the error

rates estimated using the single-exponential decay model are the averaged values over this non-constant noise. Lindblad numerical simulations (where the  $T_2^*$  process is simulated by averaging over multiple simulations with different Larmor frequencies) give non-exponential decays for RB and PB [40], agreeing with our experimental results. To reduce the non-Markovianity due to  $T_2^*$ , we implement SEL sequences before each of the benchmarking sequences, which selects a narrower line-width so the benchmarking experiments have a longer  $T_2^*$  ( $\sim 160$  ns) to begin with [40]. After incorporating the SEL sequences, the experimentally observed decays fit to a single exponential better (see the purple data points and purple dotted lines in Fig. 2). The Lindblad simulation results with the longer  $T_2^*$  also exhibit single exponential decays up to  $\sim 50$  gates [40].

Using the SEL sequence improves  $\epsilon_{\text{in}}$  from  $(6.6 \pm 0.2) \times 10^{-3}$  to  $(5.4 \pm 0.2) \times 10^{-3}$ , but has no statistically significant effect on  $\epsilon_{\text{coh}}$ , which is  $(0.9 \pm 0.4) \times 10^{-3}$  and  $(0.7 \pm 0.4) \times 10^{-3}$  with and without SEL, respectively. This implies the  $T_2^*$  effect mainly contributes to the incoherent error. In the Lindblad simulations of the benchmarking sequences using the extended  $T_2^*$ ,  $\epsilon_{\text{in}}$  caused by  $T_1$ ,  $T_2$ , and  $T_2^*$  is  $3.5 \times 10^{-3}$ , and  $\epsilon_{\text{coh}}$  caused by the imperfection in the OC pulse design is  $0.5 \times 10^{-3}$  [40]. We attribute the discrepancy between the simulated and experimental values of  $\epsilon_{\text{in}}$  and  $\epsilon_{\text{coh}}$  to possible inaccuracy in the measured decoherence times, fluctuations in the control mechanisms, and imperfect knowledge of the transfer function.

**Conclusions**– We have demonstrated how RB and PB can be used together to go beyond quantifying average gate fidelities by distinguishing coherent and incoherent contributions to the error. This allows improvements in calibration and engineering pulses to suppress incoherent errors to be implemented and diagnosed independently. Pulse distortion due to the system transfer function  $\mathcal{T}$  is the dominant error source in our system and contributes greatly to the coherent part of the gate error. Our measurement of  $\mathcal{T}$  helps improve the OC pulse fidelities significantly. The incoherent error is primarily due to  $T_1$ ,  $T_2$  and  $T_2^*$  processes. By effectively extending  $T_2^*$  we reduce the non-Markovian effect and improve the control fidelity further.

Results from gate set tomography included in the supplemental material indicate that our system has substantial gate-dependent noise. The PB protocol has only been analyzed under the assumption of gate-independent noise. Simulations using the estimates from gate set tomography indicate that PB can distinguish between gate-dependent coherent errors that look incoherent when averaged over the gates and a gate-independent incoherent process, at least for some physically-realistic error models. However, we leave the general behavior of PB under gate-dependent noise as an open problem.

**Acknowledgement** This research was supported by NSERC, the Canada Foundation for Innovation, CIFAR, the province of Ontario, Industry Canada, the Gerald Schwartz & Heather Reisman Foundation, and the U.S. Army Research Office through grant W911NF-14-1-0103. We thank David

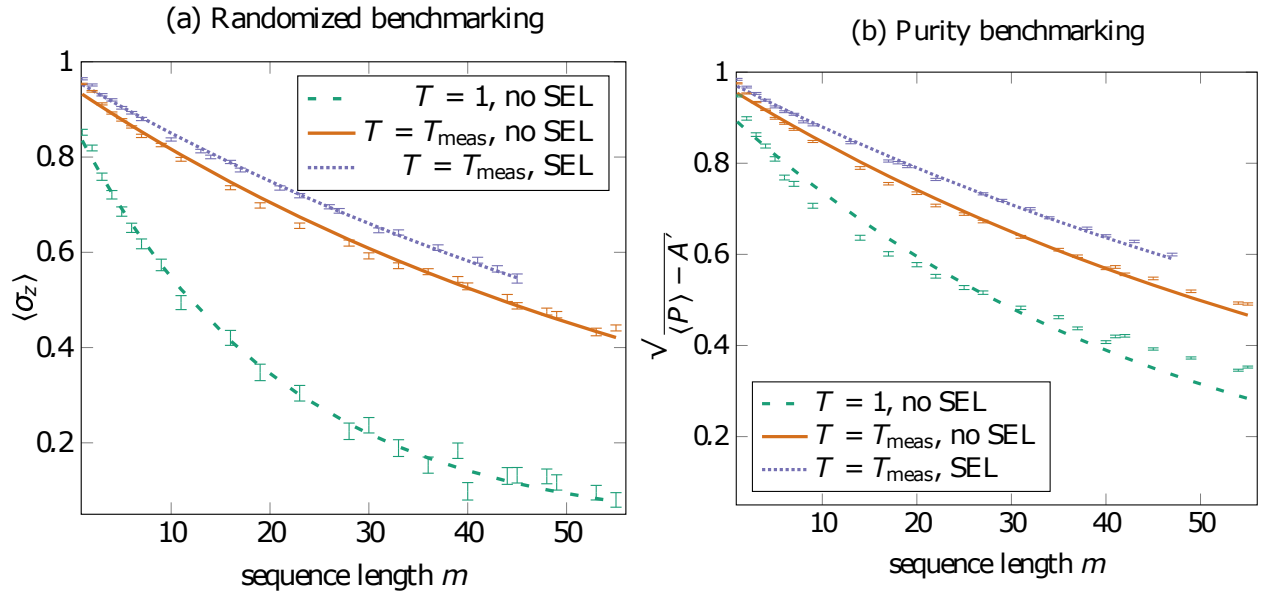


Figure 2. (Color online) Experimental (a) RB and (b) PB results. Each experimental data point of  $\langle \sigma_z \rangle$  and  $\langle P \rangle$  is an average over 150 random sequences of  $m$  Clifford gates where  $P$  is defined in Eq. (16), and the error bars indicate the standard error of the mean. The lines are least-squares fits to  $\langle \sigma_z \rangle = B(1 - 2\epsilon)^m + A_z$  and  $\langle P \rangle = B'u^{m-1} + A' = B'(1 - 2\epsilon_{\text{in}})^{2(m-1)} + A'$ , respectively.  $A_z$  are  $0.0156 \pm 0.0005$ ,  $0.0009 \pm 0.0010$  and  $-0.0004 \pm 0.0013$ , and  $A'$  are  $0.0004 \pm 0.0001$ ,  $0.0005 \pm 0.0001$  and  $0.0001 \pm 0.0001$ , for the three cases ‘ $T = 1, \text{no SEL}$ ’ (green dashed line), ‘ $T = T_{\text{meas}}, \text{no SEL}$ ’ (orange solid line), and ‘ $T = T_{\text{meas}}, \text{SEL}$ ’ (purple dotted line), respectively.  $A_z$  and  $A'$  are estimated using Eq. (18). In (b),  $\sqrt{\langle P \rangle - A'}$  is plotted instead of  $\langle P \rangle$  to show that  $\sqrt{\langle P \rangle - A'}$  has a slower decay than  $\langle \sigma_z \rangle$ , indicating  $\epsilon_{\text{in}} < \epsilon$ . The  $\epsilon$  and  $\epsilon_{\text{in}}$  values are given in Table IV. Because of the limitation of the pulsed traveling wave tube amplifier, the largest  $m$  are 55 and 47 in the cases without and with SEL sequences, respectively. All  $m$  are chosen randomly and independently for RB and PB sequences.

Cory and Troy Borneman for providing the ESR sample and for stimulating discussions; Colm Ryan, Yingjie Zhang, and Jeremy Chamilliard for their contributions to the spectrometer; Ming Lyu and Ian Hincks for the discussions on the transfer function measurement method; Robabeh Rahimi for help with preparing the ESR sample; Roberto Romero and Hiruy Haile for help with machining; Hemant Katiyar for help with the simulations.

\* baugh@uwaterloo.ca

† laflamme@iqc.ca

- [1] E. Knill, and R. Laflamme, Phys. Rev. A 55 (2), 900 (1997).
- [2] E. Knill, R. Laflamme, and W. H. Zurek, Science 279 (5349), 342–345 (1998).
- [3] J. Preskill, Proceedings of the Royal Society of London. Series A: Mathematical, Physical and Engineering Sciences 454 (1969), 385–410 (1998).
- [4] E. Knill, Nature 434 (7029), 39–44 (2005).
- [5] P. Aliferis, D. Gottesman, and J. Preskill, Quantum Information & Computation 8 (3), 181–244 (2008).
- [6] D. Gottesman, Stabilizer codes and quantum error correction. caltech ph. d, Ph.D. thesis, Thesis, eprint: quant-ph/9705052 (1997).
- [7] I. L. Chuang, and M. A. Nielsen, J. Mod. Opt. 44, 2455 (1997).
- [8] J. F. Poyatos, J. I. Cirac, and P. Zoller, Phys. Rev. Lett. 78, 390 (1997).
- [9] S. T. Merkel, J. M. Gambetta, J. A. Smolin, S. Poletto, A. D.

Córcoles, B. R. Johnson, C. A. Ryan, and M. Steffen, Phys. Rev. A 87, 062119 (2013).

- [10] R. Blume-Kohout, J. K. Gamble, E. Nielsen, J. Mizrahi, J. D. Sterk, and P. Maunz, arXiv:1310.4492 (2013).
- [11] S. Kimmel, M. P. da Silva, C. A. Ryan, B. R. Johnson, and T. Ohki, Phys. Rev. X 4, 011050 (2014).
- [12] J. Emerson, R. Alicki, and K. Życzkowski, Journal of Optics B: Quantum and Semiclassical Optics 7 (10), S347 (2005).
- [13] E. Knill, D. Leibfried, R. Reichle, J. Britton, R. B. Blakestad, J. D. Jost, C. Langer, R. Ozeri, S. Seidelin, and D. J. Wineland, Phys. Rev. A 77, 012307 (2008).
- [14] C. Dankert, R. Cleve, J. Emerson, and E. Livine, Phys. Rev. A 80 (1), 012304 (2009).
- [15] E. Magesan, J. M. Gambetta, and J. Emerson, Phys. Rev. Lett. 106, 180504 (2011).
- [16] E. Magesan, J. M. Gambetta, and J. Emerson, Phys. Rev. A 85, 042311 (2012).
- [17] J. J. Wallman, and S. T. Flammia, New J. Phys. 16, 103032 (2014).
- [18] J. J. L. Morton, A. M. Tyryshkin, A. Ardavan, K. Porfyarakis, S. A. Lyon, and G. A. D. Briggs, Phys. Rev. A 71, 012332 (2005).
- [19] S. Kimmel, G. H. Low, and T. J. Yoder, Phys. Rev. A 92, 062315 (2015).
- [20] Y. R. Sanders, J. J. Wallman, and B. C. Sanders, New J. Phys. 18, 012002 (2015).
- [21] J. J. Wallman, M. Barnhill, and J. Emerson, Phys. Rev. Lett. 115, 060501 (2015).
- [22] P. J. J. O’Malley *et al.*, Phys. Rev. Appl. 3, 044009 (2015).
- [23] J. J. Wallman, C. Granade, R. Harper, and S. T. Flammia, New J. Phys. 17, 113020 (2015).
- [24] S. Sheldon *et al.*, Phys. Rev. A 93, 012301 (2016).

- [25] J. J. Wallman, arXiv:1511.00727 (2015).
- [26] R. Kueng, D. M. Long, A. C. Doherty, and S. T. Flammia, arXiv:1510.05653 (2015).
- [27] T.W. Borneman, C.E. Granade, D.G. Cory, Phys. Rev. Lett. 108 (14), 140502 (2012).
- [28] J. S. Hodges, J. C. Yang, C. Ramanathan, and D. G. Cory, Phys. Rev. A 78 (1), 010303 (2008).
- [29] Y. Zhang, C. A. Ryan, R. Laflamme, and J. Baugh, Phys. Rev. Lett. 107 (17), 170503 (2011).
- [30] D. K. Park, G. Feng, R. Rahimi, S. Labruyère, T. Shibata, S. Nakazawa, K. Sato, T. Takui, R. Laflamme, and J. Baugh, Quantum Information Processing 14 (7), 2435–2461 (2015).
- [31] T. Prisner, M. Rohrer, and F. MacMillan, Annu. Rev. Phys. Chem. 52, 279 (2001).
- [32] P.E. Spindler, Y. Zhang, B. Endeward, *et al.*, J. Magn. Reson. 218, 49 (2012).
- [33] N. Khaneja, T. Reiss, C. Kehlet, T. Schulte-Herbrüggen, and S. J. Glaser, Journal of Magnetic Resonance 172, 296–305 (2005).
- [34] D. K. Park, G. Feng, R. Rahimi, J. Baugh, and R. Laflamme, Journal of Magnetic Resonance 267, 68 (2016).
- [35] C. King, and M. B. Ruskai, J. Math. Phys. 42, 87 (2001).
- [36] M. B. Ruskai, S. Szarek, and E. Werner, Linear Algebr. Appl. 347 159 (2002).
- [37] S. Eaton, and G. Eaton, Journal of Magnetic Resonance, Series A 102 354 – 356 (1993).
- [38] T. Kaufmann *et al.*, J. Magn. Reson. 235, 95 (2013).
- [39] S. Gustavsson, O. Zwier, J. Bylander, F. Yan, F. Yoshihara, Y. Nakamura, T. P. Orlando, and W. D. Oliver, Phys. Rev. Lett. 110, 040502 (2013).
- [40] See Supplemental Material, which includes Ref. [41], for details of the transfer function measurement, optimal control pulse design, gate set tomography results, and simulations.
- [41] J. M. Chow *et al.*, Phys. Rev. Lett. 109, 060501 (2012).
- [42] C. A. Ryan, M. Laforest, and R. Laflamme, New J. of Phys. 11 (1), 013034 (2009).
- [43] M. A. Fogarty, M. Veldhorst, R. Harper, C. H. Yang, S. D. Bartlett, S. T. Flammia, and A. S. Dzurak, Phys. Rev. A 92, 022326 (2015).

## Supplementary Material: Estimating the coherence of noise in quantum control of a solid-state qubit

### Determination of the system transfer function

In order to characterize our transfer function, we measure Rabi oscillations of the spin signal under microwave pulses across a set of offset frequencies. By numerically fitting the measured oscillations to a theoretical model, the amplitude and phase of the transfer function are obtained.

First, we consider the Hamiltonian of the single-qubit system in the lab frame:

$$H_{\text{lab}} = H_0 + H_{\text{mw}} = \omega_0 \frac{\sigma_z}{2} + \Omega \frac{\sigma_x}{2} \cos(\omega(t - t_0) + \psi), \quad (\text{S1})$$

where  $H_0$  is the Zeeman interaction between the electron spin and the static magnetic field and  $H_{\text{mw}}$  is the interaction between the electron spin and the microwave field. Using the rotating-wave approximation (RWA), the Hamiltonian in the rotating frame with frequency  $\omega$  has the following form:

$$H_{\text{RWA}} = -\Delta \frac{\sigma_z}{2} + \Omega \left( \frac{\sigma_x}{2} \cos(\psi) + \frac{\sigma_y}{2} \sin(\psi) \right), \quad (\text{S2})$$

where  $\Delta = \omega - \omega_0$ ,  $\Omega$ , and  $\psi$  are the offset frequency, amplitude, and phase of the microwave pulse, respectively. Here, we consider a constant  $\Omega$  for simplicity which means the microwave pulse has a single frequency component  $\omega$ .  $\Omega \cos(\psi)$  and  $\Omega \sin(\psi)$  are always referred to as in-phase part (denoted as  $\mathcal{W}_0$ ) and quadrature part (denoted as  $\mathcal{W}_{90}$ ). This allows the waveform to be conveniently written in a complex form of  $\mathcal{W}_0 + i\mathcal{W}_{90} = \Omega e^{i\psi}$ . Distortion caused by the finite bandwidth of the resonator and imperfections in microwave generation and transmission makes  $\Omega e^{i\psi}$  different from the intended waveform  $\Omega_0 e^{i\psi_0}$ . The ratio  $\Omega e^{i\psi} / (\Omega_0 e^{i\psi_0})$  is the value of the transfer function  $\mathcal{T}$  at offset frequency  $\Delta$ . Therefore,  $\mathcal{T}$  can be obtained by measuring  $\Omega e^{i\psi} / (\Omega_0 e^{i\psi_0})$  at different offset frequencies.

Equation (S2) shows that in the rotating frame with frequency  $\omega$ , the spin polarization is rotating at the frequency  $\omega_1 = \sqrt{\Delta^2 + \Omega^2}$  around the axis  $\hat{n} = (\frac{\Omega}{\omega_1} \cos(\psi), \frac{\Omega}{\omega_1} \sin(\psi), -\frac{\Delta}{\omega_1})$  (Fig. 3). The initial state of  $\sigma_z$  evolves as:

$$\begin{aligned} \rho(t) = & \left( \cos^2\left(\frac{\omega_1(t-t_0)}{2}\right) + \sin^2\left(\frac{\omega_1(t-t_0)}{2}\right) \cos 2\theta \right) \sigma_z \\ & + \left( \sin^2\left(\frac{\omega_1(t-t_0)}{2}\right) \right) \sin 2\theta \cos \psi \\ & + \sin(\omega_1(t-t_0)) \sin \theta \sin \psi \sigma_x \\ & + \left( \sin^2\left(\frac{\omega_1(t-t_0)}{2}\right) \right) \sin 2\theta \sin \psi \\ & - \sin(\omega_1(t-t_0)) \sin \theta \cos \psi \sigma_y, \end{aligned} \quad (\text{S3})$$

where  $\sin \theta = \frac{\Omega}{\omega_1}$  and  $\cos \theta = -\frac{\Delta}{\omega_1}$ . In our experiments, it is more convenient to work in the rotating frame of frequency  $\omega_0$ , where the evolution of expectation values  $\langle \sigma_x(t) \rangle$

and  $\langle \sigma_y(t) \rangle$  can be expressed as:

$$\langle \sigma_x(t) \rangle = \text{Tr}(\sigma_x e^{i(t-t_0)\Delta\sigma_z/2} \rho(t) e^{-i(t-t_0)\Delta\sigma_z/2}) \quad (\text{S4})$$

$$\langle \sigma_y(t) \rangle = \text{Tr}(\sigma_y e^{i(t-t_0)\Delta\sigma_z/2} \rho(t) e^{-i(t-t_0)\Delta\sigma_z/2}). \quad (\text{S5})$$

We applied constant amplitude pulses at frequency  $\omega$  and fitted the experimental oscillations of  $\langle \sigma_x(t) \rangle$  and  $\langle \sigma_y(t) \rangle$  to Eqs. (S4) and (S5) (see Fig. 4) to extract  $\psi$  and  $\Omega$ . By varying  $\omega$ , we can obtain estimates of  $\Omega e^{i\psi} / (\Omega_0 e^{i\psi_0})$  at different frequencies.

There are two issues of the method described above that need to be addressed. First, the method assumes the input microwave pulse with constant amplitude and single frequency component  $\omega$ . However, in real systems the pulses will have a rising and falling at the beginning and end, during which the spin experiences varying microwave field. If the rising and falling time is very short compared to the total pulse length, the effect can be neglected to a good approximation. In our system, due to the finite bandwidth of the resonator as well as limitations in the transmission components (*e.g.*, IQ mixer and amplifier), the rising and falling time of a pulse is around 5~10 ns, which is non-negligible for short pulses. To reduce the effect of the rising and falling of the pulse, we used relatively long pulses (>120 ns). By fitting Rabi oscillations assuming the pulses are perfect pulses with constant amplitude, we obtained an initial guess for the transfer function (denoted as  $\mathcal{T}_0$ ). In the next fitting iteration, we simulated the Rabi oscillations due to the pulses distorted by  $\mathcal{T}_0$ . In this way, we minimize the effect of imperfect pulses and obtained a refined transfer function. Another issue is that the fitting results of the phase part of the transfer function,  $\psi(\omega)$ , strongly depend on the choice of the starting time point  $t_0$ . From Eq. (S1), it is not difficult to prove that with a temporal shift  $\delta t$  relative to  $t_0$ ,  $\psi(\omega)$  will get an additional slope which is  $\delta t \omega$ . Due to the distortion of the pulses, there is uncertainty in determining  $t_0$ . To compensate, we used the refined fitting result of the transfer function as an initial guess to modify our optimal control (OC) pulses and measured the average gate fidelity using randomized benchmarking (RB). We then performed a few iterations of feed-back control where we slightly adjusted the slope of the phase of the transfer function (and our OC pulses accordingly) until we maximized our average gate fidelity and got the measured transfer function  $\mathcal{T}_{\text{meas}}$  as shown in Fig. 5. The gate set tomography (GST) results of unmodified OC pulses, the OC pulses modified by  $\mathcal{T}_{\text{meas}}$ , and the OC pulses modified by  $|\mathcal{T}_{\text{meas}}|$  are given in Table II. The table clearly shows both the amplitude and phase of the transfer function are important in improving the fidelities of the OC pulses.

It should be noted that  $\mathcal{T}_{\text{meas}}$  becomes inaccurate when the offset frequency  $\Delta$  is large, as the fitting of the experimental Rabi oscillations is less sensitive to the microwave pulse amplitude and phase when  $|\Omega/\Delta|$  is small. However, because the

excitation bandwidths of our OC pulses are about 100 MHz or less, the imperfections of  $\mathcal{T}_{\text{meas}}$  for  $|\Delta|$  larger than the bandwidths does not affect the controls of the OC pulses significantly. From the experimental results shown in the main text and the results listed in Table II, correcting the OC pulses using  $\mathcal{T}_{\text{meas}}$  obtained by the method described above improves the control fidelities greatly. Therefore, we conclude that our  $\mathcal{T}_{\text{meas}}$  is a good estimate of the system transfer function  $\mathcal{T}$  within the bandwidths of the OC pulses.

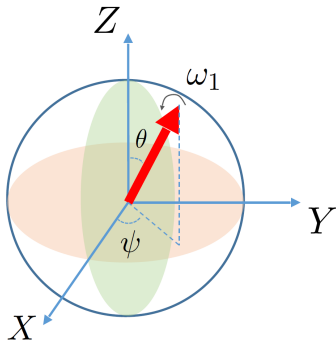


Figure 3. (Color online) The red arrow is the rotation axis  $(\sin(\theta) \cos(\psi), \sin(\theta) \sin(\psi), \cos(\theta))$  of the spin polarization under the Hamiltonian in Eq. (S2).

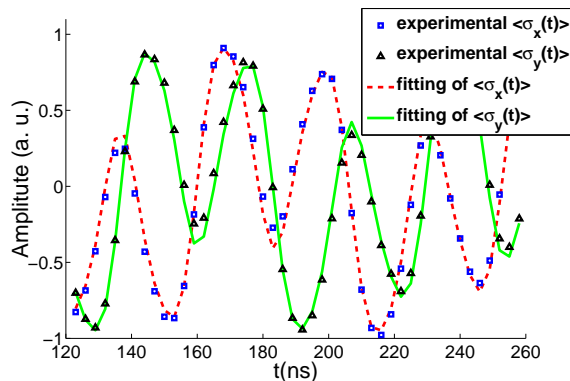


Figure 4. (Color online) Experimental and fitted trajectories of  $\langle \sigma_x(t) \rangle$  and  $\langle \sigma_y(t) \rangle$  at offset frequency  $\Delta = 32$  MHz.

#### Schematic diagram of experimental setup

Figure 6 shows the schematic diagram of the home-built pulsed X-band electron spin resonance (ESR) spectrometer used for the experiments presented in the paper. First, the signal source (Rhode & Schwarz) generates continuous-wave reference microwave signal of  $\sim 10$  GHz, which is split into two by the two-way splitter (Marki). For the transmission, pulses with desired amplitudes and phases are constructed by up-converting the reference using the IQ mixer (Marki) and the arbitrary waveform generator (Tektronix) which has maximum resolution of 1 ns. Typical intermediate frequency (IF)

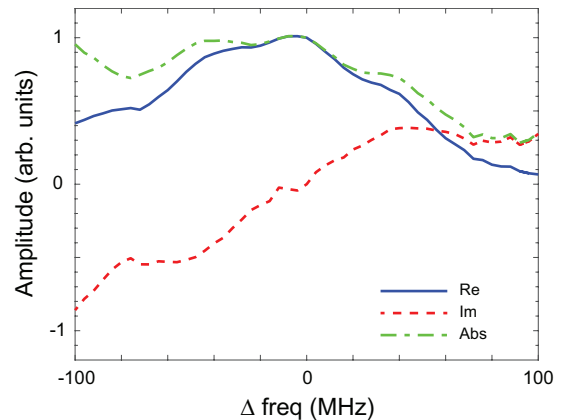


Figure 5. (Color online) The measured transfer function,  $\mathcal{T}_{\text{meas}}$ , as a function of offset frequency relative to the resonant frequency  $\omega_0 = 9.996$  GHz.

fed into the IQ ports for the up-conversion is from 150 to 200 MHz. Next the pulses enter the microwave resonator located at the center of the water-cooled electromagnet through a series of attenuator (Advanced Technical Materials) and amplifiers (pre-amplifier: MITEQ; pulsed traveling wave tube amplifier: applied system engineering) to achieve appropriate amplifications, followed by circulators (DiTom) to minimize unwanted reflections.

Spin signals are directed to the receiver which consists of the limiter (Pasternack), fast PIN diode switch (Advanced Technical Materials), filters (Mini-circuits), low-noise amplifier (MITEQ), circulator (DiTom), and front-end receiver mixer (MITEQ). The limiter and PIN switch are implemented to prevent too much power flooding into the low-noise amplifier, and the high-pass filter (Mini-Circuits) blocks the low-frequency transient responses of the switching on and off. The circulator also protects the low-noise amplifier from unwanted reflections as well as possible leakage of the reference through the receiver mixer. Finally another filtering stage (Mini-Circuits) removes artifacts from the receiver mixer, and the spin signals, down-converted to the same IF frequency used in the up-conversion scheme, are captured by a fast digital oscilloscope (LeCroy). Further signal processing, *i.e.*, down-conversion to d.c., is performed by a computer. More details about the spectrometer can be found in Ref. [34].

#### Correction of non-linear amplitude fluctuation and phase droop of pulsed TWT amplifier

As we reported in Ref. [34], the raw output from the pulsed traveling wave tube (TWT) amplifier in our setup can be non-linear (both in amplitude and phase; mainly due to heating of the amplifier) across the desired pulse sequence period. In RB and purity benchmarking (PB) experiments where we extend the sequences nearly to the maximum pulse sequence duration ( $\sim 15 \mu\text{s}$ ) limited by the pulsed TWT amplifier, we corrected

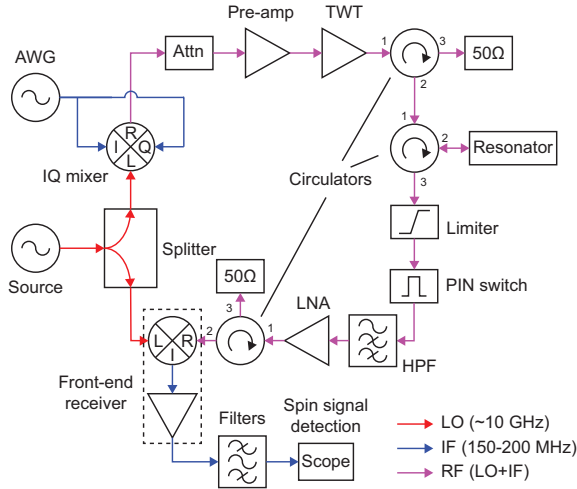


Figure 6. (Color online) Schematic diagram of the home-built pulsed X-band ESR spectrometer. Abbreviations used in the diagram are: AWG, arbitrary waveform generator; Attn, attenuator; Pre-amp, pre-amplifier; TWT, traveling wave tube amplifier; HPF, high-pass filter; LNA, low-noise amplifier. Red arrows (LO) denote the reference microwave frequency generated by the source, blue arrows (IF) denote the frequency of the signals from the arbitrary waveform generator going to the IQ mixer for the up-conversion (spin signals have the same frequency after the down-conversion by the front-end receiver mixer), and purple arrows denote the frequency of up-converted signal.

the non-linear amplitude fluctuation and phase droop in order to achieve the best control fidelities. The non-linearity was corrected using a technique similar to how the transfer function was used to pre-distort the OC pulses. We first measure the TWT amplifier’s output when a long square pulse was input in order to observe the amplitude non-linearity and phase droop as a function of time. We can feed back this information to pre-distort the input pulse sequences. After this process, the majority of non-linearity and phase droop is corrected as shown in Fig. 7.

### Larmor frequency distribution and $B_1$ field distribution

The Larmor frequency distribution and  $B_1$  field distribution, measured by detecting the spin signals, are the properties of the combined system of the sample and the resonator (Figs. 8 and 9). In particular, the asymmetric shape of the Larmor frequency distribution is mainly due to the anisotropy of the  $g$ -value of the electron spins in the irradiated fused quartz sample.

### Optimal control pulses

We designed three OC pulse shapes to realize  $\pi/2$  and  $\pi$  rotations around  $x$  and  $y$ -axes and an identity operation. Different rotation axes for the  $\pi/2$  and  $\pi$  pulses were realized

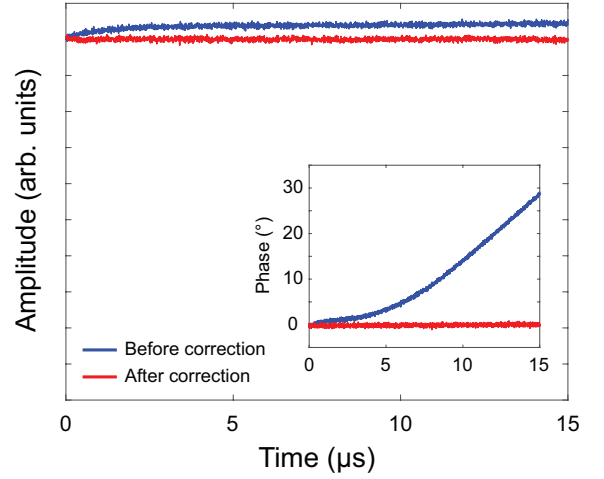


Figure 7. (Color online) Amplitude of a long square pulse output by the TWT amplifier before and after correction measured by a directional coupler. Inset shows the phase droop. In all of the experiments, a waiting time of  $2 \mu\text{s}$  after unblinking the TWT is employed to allow the output to stabilize (not shown).

	$F(X90)$	$F(Y90)$	$F(X180)$	$F(Y180)$	$F(\mathcal{I})$
$\mathcal{T} = \mathcal{T}_{\text{meas}}$ , SEL	$0.9940^{+24}_{-42}$	$0.9969^{+12}_{-45}$	$0.9926^{+29}_{-43}$	$0.9932^{+25}_{-41}$	$0.9890^{+33}_{-44}$
$\mathcal{T} = \mathcal{T}_{\text{meas}}$ , no SEL	$0.9914^{+19}_{-26}$	$0.9926^{+23}_{-29}$	$0.9916^{+19}_{-31}$	$0.9924^{+26}_{-31}$	$0.9838^{+33}_{-26}$
$\mathcal{T} = 1$ , no SEL	$0.9785^{+41}_{-113}$	$0.9790^{+50}_{-98}$	$0.9796^{+60}_{-130}$	$0.9773^{+48}_{-124}$	$0.9588^{+102}_{-114}$
$\mathcal{T} =$ $ \mathcal{T}_{\text{meas}} $ , no SEL	$0.9915^{+33}_{-57}$	$0.9912^{+29}_{-50}$	$0.9910^{+36}_{-50}$	$0.9900^{+33}_{-50}$	$0.9765^{+45}_{-60}$
5% miscal, $\mathcal{T} = \mathcal{T}_{\text{meas}}$ , no SEL	$0.9880^{+28}_{-36}$	$0.9892^{+21}_{-35}$	$0.9906^{+24}_{-35}$	$0.9911^{+33}_{-34}$	$0.9811^{+36}_{-34}$
-5% miscal, $\mathcal{T} = \mathcal{T}_{\text{meas}}$ , no SEL	$0.9906^{+22}_{-35}$	$0.9924^{+24}_{-31}$	$0.9911^{+26}_{-30}$	$0.9913^{+26}_{-32}$	$0.9819^{+32}_{-32}$

Table II. Fidelity  $F$  (Eq. (1)) from GST results under different experimental conditions. ‘ $\mathcal{T} = \mathcal{T}_{\text{meas}}$ ’ and ‘ $\mathcal{T} = |\mathcal{T}_{\text{meas}}|$ ’ denote the cases of OC pulses modified by taking into account  $\mathcal{T}_{\text{meas}}$  and  $|\mathcal{T}_{\text{meas}}|$ , respectively. ‘ $\mathcal{T} = 1$ ’ denotes the case of unmodified OC pulses. ‘SEL’ stands for the spin-packet selection sequences. ‘5% miscal’ and ‘-5% miscal’ denote the cases when implementing OC pulses with powers that are 5% larger and smaller than the calibrated pulse power, respectively. The error bars are calculated using the best and worst process matrices when sampling the parameters of the process matrices within two standard deviations under the CPTP constraints.

through phase shifting. X90 and Y90 denote a  $\pi/2$  pulse about the  $x$ - and  $y$ -axes, X180 and Y180 denote a  $\pi$  pulse about the  $x$ - and  $y$ -axes, and  $\mathcal{I}$  denotes an identity pulse. We used the gradient ascent pulse engineering algorithm [33] to design OC pulses. In our system,  $T_2^* < 100 \text{ ns}$  is the shortest time scale at which decoherence occurs. To make the OC pulses robust to  $T_2^*$  noise, the weighted average fidelity over the Larmor frequency distribution (Fig. 8) is numerically optimized. Furthermore, OC pulses are made to be robust to the inhomogeneity in the microwave field (Fig. 9) using the same

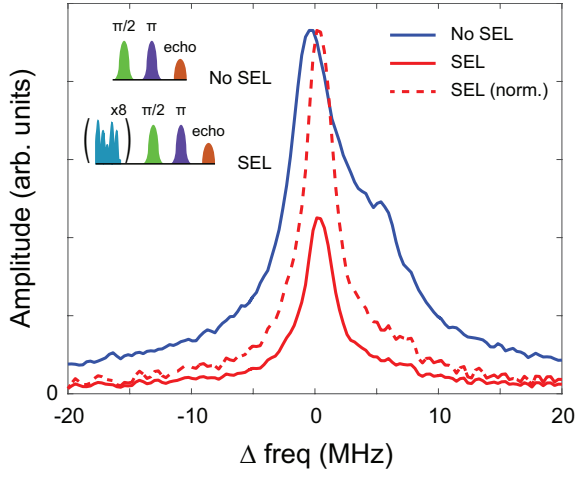


Figure 8. (Color online) Thermal spectrum (Larmor frequency distribution profile) with and without the spin-packet selection (SEL) sequence. With the SEL sequence, the linewidth narrows by about half, but at the same time, more than half of the amplitude is lost (the dotted line which represents the spectrum with SEL sequence that is normalized to the spectrum without SEL sequence). The inset shows the pulse sequences used to measure the corresponding spectra. For SEL, a numerically derived  $2\pi$  pulse that is not robust to Larmor frequency distribution is repeated eight times and each separated by an order of  $T_2$  before the spin echo readout.

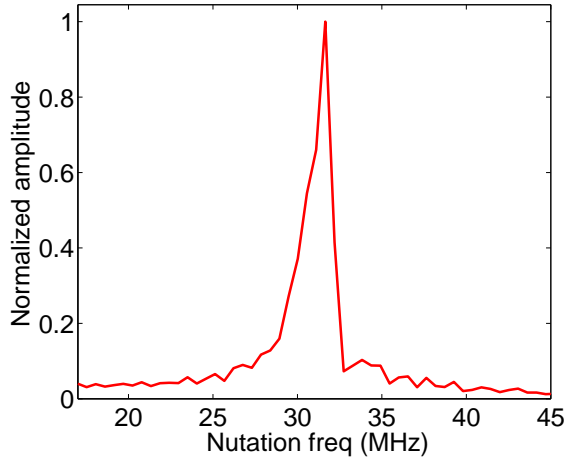


Figure 9. (Color online)  $B_1$  distribution profile obtained by taking the Fourier transform of the experimental Rabi oscillations, and refined by comparing the experimental and simulated Rabi oscillations [34]. The FWHM is about 1.7 MHz.

method.

Table III gives the weighted average fidelity (Eq. (1)) of each OC pulse under different numerical simulation conditions ( $T_1$  and  $T_2$  effects are not considered here), and it shows the ideal OC pulses should be very robust to  $T_2^*$  noise and power mis-calibration. However, in the experiments, when the OC pulses arrive at the spins, they are distorted by the system transfer function. To investigate the effect of the system transfer function on the OC pulse fidelities, we use  $\mathcal{T}_{\text{meas}} \cdot W$

to approximately simulate the distorted OC pulses, and the fidelities are presented in Table III. It shows that the coherent error of the pulses increases greatly, and the incoherent error also increases because the pulses lose part of the designed robustness to the  $T_2^*$  noise and  $B_1$  field distribution due to the transfer function.

The experimental fidelities of the OC pulses are given in Table II. After using the measured transfer function  $\mathcal{T}_{\text{meas}}$  to modify the pulses to compensate the effect of the system transfer function in experiment, despite the imperfection of  $\mathcal{T}_{\text{meas}}$ , the pulses remain somewhat robust to these inhomogeneities.

	$F(X90)$	$F(X180)$	$F(\mathcal{I})$	$\epsilon_{oc}$	$\epsilon_{oc,in}$
$T_2^* \sim 160$ ns	0.9985	0.9995	0.9992	0.0009	0.0006
$T_2^* \sim 80$ ns	0.9976	0.9975	0.9974	0.0025	0.0021
5% miscal, $T_2^* \sim 80$ ns	0.9985	0.9974	0.9972	0.0023	0.0019
-5% miscal, $T_2^* \sim 80$ ns	0.9951	0.9982	0.9935	0.0044	0.0039
Distorted, $T_2^* \sim 80$ ns	0.9822	0.9871	0.9615	0.0230	0.0113

Table III. Fidelity  $F$  (Eq. (1)),  $\epsilon_{oc}$  and  $\epsilon_{oc,in}$  from numerical simulations ( $T_1$  and  $T_2$  effects are not considered).  $\epsilon_{oc}$  and  $\epsilon_{oc,in}$  are the average BEPG and IEPG of the three OC pulses.  $F(X90)$  and  $F(Y180)$  are the same as  $F(X90)$  and  $F(X180)$ , respectively. ' $T_2^* \sim 160$  ns' and ' $T_2^* \sim 80$  ns' denote the cases when simulating using the Larmor frequency distributions that correspond to the experiments with and without SEL, respectively. '5% miscal' and '-5% miscal' denote the cases when simulating OC pulses with powers that are 5% larger and smaller than the ideal pulse power, respectively. 'Distorted' denotes the case where the distorted OC pulses ( $\mathcal{T}_{\text{meas}} \cdot W$ ) are simulated. The  $T_2^*$  values are estimated from the experimentally measured spectra using a single Lorentzian line shape. In our numerical simulations, we try to more closely match the measured spectra by using Larmor frequency distributions composed of multiple Lorentzian and/or Gaussian line shapes instead of just one.

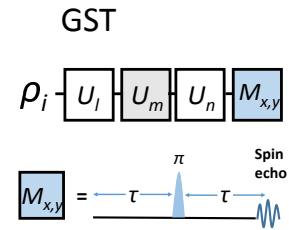


Figure 10. (Color online) Quantum circuit for performing GST. In all experiments, the initial state  $\rho_i$  is  $\sigma_z$  and the measurements  $M_{x,y}$  are spin echo detection sequences for measuring  $\langle \sigma_{x,y} \rangle$ . In  $M_{x,y}$ , the  $\pi$  pulse is a 35 ns Gaussian pulse around the  $y$ -axis, and  $\tau=700$  ns represents a delay. The  $\pi$  pulse acts as the refocusing pulse. The spin echo appears at time  $\tau$  after the refocusing pulse and the spin magnetization in the  $x$ - $y$  plane is detected inductively.

### Gate set tomography

		Experimental short sequences of RB/PB	GST simulation of RB/PB	GST estimates A	GST estimates B
$\mathcal{T} = \mathcal{T}_{\text{meas}},$	$\epsilon$	0.0081(29)	0.0086(1)	$0.0084_{-31}^{+57}$	–
	SEL $\epsilon_{\text{in}}$	0.0078(8)	0.0076(0)	$0.0076_{-31}^{+57}$	$0.0084_{-31}^{+57}$
$\mathcal{T} = \mathcal{T}_{\text{meas}},$	$\epsilon$	0.0113(33)	0.0124(1)	$0.0121_{-30}^{+38}$	–
	no SEL $\epsilon_{\text{in}}$	0.0101(17)	0.0111(1)	$0.0111_{-30}^{+38}$	$0.0120_{-30}^{+38}$
$\mathcal{T}=1,$	$\epsilon$	0.0285(105)	0.0331(4)	$0.0331_{-76}^{+151}$	–
	no SEL $\epsilon_{\text{in}}$	0.0205(78)	0.0247(3)	$0.0250_{-71}^{+150}$	$0.0331_{-76}^{+151}$

Table IV. BEPG  $\epsilon$  and IEPG  $\epsilon_{\text{in}}$  per Clifford gate under different conditions. ‘ $\mathcal{T}=1$ , no SEL’ denotes the case of unmodified OC pulses; ‘ $\mathcal{T} = \mathcal{T}_{\text{meas}}$ , SEL’ and ‘ $\mathcal{T} = \mathcal{T}_{\text{meas}}$ , no SEL’ denote the cases of OC pulses modified by taking into account  $\mathcal{T}_{\text{meas}}$  with and without the spin packet selection sequence (SEL), respectively. The first column gives the values derived from experimental decays of the RB and PB sequences with 1~4 Clifford gates. The second column gives the values derived from the simulated decays of the RB and PB sequences with up to 55 Clifford gates, using the process matrices derived in GST experiments. The third and fourth columns give the values calculated from  $\mathbf{G} = \mathcal{SPZ}$  using the process matrices reconstructed by GST. The error bars in the first and second columns come from the fitting to the models in Eq. (17) of the main text and indicate the 95% confidence interval. The error bars in the third and fourth columns are calculated using the best and worst process matrices when sampling the parameters of the process matrices within two standard deviations under the CPTP constraints. The  $\epsilon_{\text{in}}$  in the third and fourth columns are calculated using  $\epsilon_{\text{in}} = (1 - \sqrt{\text{av}u})/2$  and  $\epsilon_{\text{in}} = (1 - \sqrt{u_{\text{av}}})/2$ , where  $\text{av}u$  and  $u_{\text{av}}$  are defined in Eqs. (S7) and (S8), respectively. Both  $\epsilon$  and  $\epsilon_{\text{in}}$  in the third column agree with the values in the second column, indicating the robustness of RB and PB to the realistic gate-dependent noise. The  $\epsilon_{\text{in}}$  in the fourth column deviate from the values in the second column, indicating PB gives the average of the unitarities ( $\text{av}u$ ) instead of the unitarity of the average noise ( $u_{\text{av}}$ ).

The RB and PB protocols assume that the noise has little or no gate dependence, which is likely violated in real systems. To study the robustness of RB and PB to gate-dependent noise, we also implement GST [9, 10] to reconstruct the process matrices of the OC pulses and use them to compare with the benchmarking results. Compared to standard quantum process tomography (QPT), GST is more robust to state preparation and measurement (SPAM) errors and thus provides more accurate information about the target gates. GST is implemented by applying three operations  $U_l, U_m, U_n \in \{\text{X90}, \text{Y90}, \text{X180}, \text{Y180}, \mathcal{I}\}$  to  $\rho_i = \sigma_z$  and measuring  $\langle \sigma_x \rangle$  and  $\langle \sigma_y \rangle$  (see Fig. 10). The Pauli process matrices [41] of the OC pulses are then estimated by minimizing the variance between the estimated and experimental values of

$\langle \sigma_x \rangle$  and  $\langle \sigma_y \rangle$  [9]. Let  $\mathcal{Q}^{\text{exp}} = \{Q_1, Q_2, Q_3, Q_4, Q_5\}$  denote the Pauli process matrices of the experimentally-implemented  $\{\text{X90}, \text{Y90}, \text{X180}, \text{Y180}, \mathcal{I}\}$  pulses and  $\mathbf{m}_{k,lmn}$  denote the expectation value of  $\sigma_k$  after applying  $U_l, U_m, U_n$ . We estimate the Pauli process matrices by measuring the expectation values for each of the 125 combinations of the OC pulses and minimizing

$$LSQ(\mathcal{Q}) = \sum_{k,l,m,n} |\mathbf{m}_{k,lmn} - \langle \langle M_k | Q_l Q_m Q_n | \rho_i \rangle \rangle|^2, \quad (\text{S6})$$

$$k = x, y; l, m, n = 1, \dots, 5$$

under the constraint that the noise is completely-positive and trace-preserving (CPTP) [9]. Here,  $\langle \langle M_k |$  and  $| \rho_i \rangle \rangle$  are the vector forms of the measurement operator  $M_k$  ( $k = x, y$ ) and initial state  $\rho_i$ , whose elements are  $\langle \langle M_k | \sigma_j \rangle \rangle = \text{Tr}[M_k \sigma_j]$  and  $\langle \langle \sigma_j | \rho_i \rangle \rangle = \text{Tr}[\rho_i \sigma_j]/2$  with  $\sigma_j \in \{\mathbb{1}_2, \sigma_x, \sigma_y, \sigma_z\}$  ( $j = 1, 2, 3, 4$ ).

The estimated process matrices for the OC pulses are given in the next section and their fidelities are given in Table II. We then use these measured process matrices to construct the process matrices of Clifford gates from  $\mathbf{G} = \mathcal{SPZ}$  ( $\mathcal{S} \in \{\mathcal{I}, \text{X90}, \text{Y90}\}$ ,  $\mathcal{P} \in \{\mathcal{I}, \text{Y180}\}$ , and  $\mathcal{Z} \in \{\mathcal{I}, \text{Z90}, \text{Z180}, \text{Z270}\}$ ) and calculate the benchmarking average error per gate (BEPG)  $\epsilon$ , which are listed in the ‘GST estimates A’ column of Table IV. We found that the calculated  $\epsilon$  values are closer to the fitting results of the first few gates of the experimental data within error bars than the fitting results obtained by including all gates in the RB and PB sequences (*i.e.* values listed in Table I of the main text). We believe this is due to the GST sequences containing only three gates, which are not appropriate to predict the asymptotic behaviour of the RB and PB sequences (also see Fig. 11).

We also use two different methods to calculate the incoherent error per gate (IEPG)  $\epsilon_{\text{in}}$  using the process matrices derived from GST. The PB protocol has only been analyzed under the assumption that the noise is gate-independent. One immediate question is whether the decay parameter of PB should be the average of the unitarities of the gate-dependent noise,

$$\text{av}u = |\mathbf{G}|^{-1} \sum_{G \in \mathbf{G}} u[\mathcal{E}(G)], \quad (\text{S7})$$

or the unitarity of the average noise,

$$u_{\text{av}} = u \left[ |\mathbf{G}|^{-1} \sum_{G \in \mathbf{G}} \mathcal{E}(G) \right]. \quad (\text{S8})$$

These two quantities are not equal in general, as the unitarity is not a linear function of quantum channels. The IEPG for both quantities are listed in columns ‘GST estimates A’ and ‘GST estimates B’ of Table IV. Although the table shows that  $\text{av}u$  is closer to the experimentally observed decay than  $u_{\text{av}}$ , the error bars are large and we cannot get statistically meaningful conclusion whether the PB protocol measures the average of the incoherent errors of the gate-dependent noise

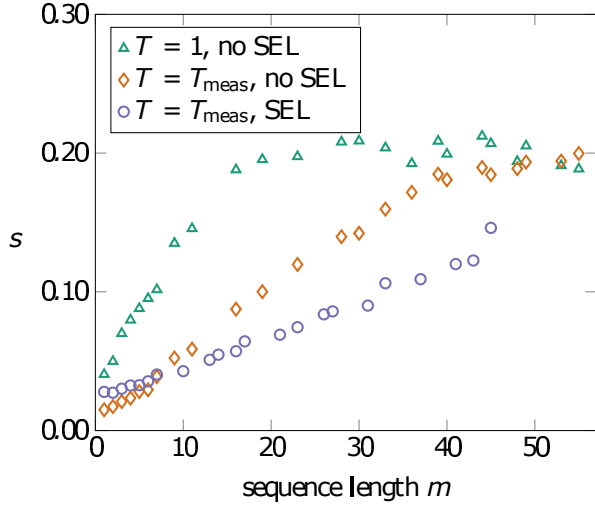


Figure 11. (Color online) Standard deviation  $s$  between experimental RB results and GST simulations of the expectation values over 150 random sequences. The results of the three conditions, using the unmodified OC pulses, the transfer function modified OC pulses and the transfer function modified OC pulses with SEL, are presented by green triangles, orange diamonds, and purple circles, respectively. The increase of  $s$  with the sequence length can be attributed to the fact that GST was performed using sequences of three pulses, which limits the accuracy. Up to the first few gates, the GST simulations agree closely with each individual sequence of the RB experiments for the modified OC pulses, but demonstrate substantial disagreement for the unmodified pulses. We attribute this disagreement to inaccuracies of the GST results in characterizing the large coherent errors in the individual gates resulting from the uncorrected distortion. For the OC pulses modified by the transfer function with SEL, the  $s$  values are unexpectedly higher (compared to no SEL) for the first few gates. We attribute this mainly to a smaller signal-to-noise ratio in the case of SEL. Note that the roughly linear increases in  $s$  versus sequence length suggest that discrepancies are accumulating stochastically rather than coherently.

or the incoherent error of the noise averaged over the gates being benchmarked.

Therefore, we use the help of simulation to further study the performance of PB and RB. We use the experimental GST process matrices as realistic noise models to simulate RB and PB with the same sequences used in the experiment (up to 55 Clifford gates). The derived decay rates of the simulations are listed in the column ‘GST simulation of RB/PB’ of Table IV. The values in the ‘GST simulation of RB/PB’ and in the ‘GST estimates A’ agree to within the fitting uncertainty (note that the uncertainties in the ‘GST estimates A’ and ‘GST estimates B’ are not relevant as our simulations are of the average GST reconstructions), indicating that under realistic noise models consistent with our system, both the RB and PB work very well in estimating the BEPG and IEPG. Furthermore, our simulations suggest the PB protocol measures the average of the incoherent errors of the gate-dependent noise, which is sensitive to individual calibration errors (even if these gate-dependent calibration errors average into an incoherent process).

### Gate set tomography results

Here we list the reconstructed Pauli transfer matrices obtained from the GST experiments. There are three cases: (i) OC pulses are modified by  $\mathcal{T}_{\text{meas}}$  and SEL is used; (ii) OC pulses are modified by  $\mathcal{T}_{\text{meas}}$  and no SEL; (iii) unmodified pulses and no SEL.

In case (i):

$$X_{90} = \begin{bmatrix} 1 & 0 & 0 & 0 \\ -0.0037 & 0.9886 & -0.0249 & 0.0112 \\ -0.0051 & 0.0102 & 0.0451 & -0.9899 \\ 0.0021 & 0.0204 & 0.9857 & 0.0495 \end{bmatrix},$$

$$Y_{90} = \begin{bmatrix} 1 & 0 & 0 & 0 \\ 0.0053 & 0.0511 & -0.0152 & 0.9925 \\ 0.0035 & 0.0163 & 0.9947 & 0.0121 \\ 0.0011 & -0.9939 & 0.0167 & 0.0510 \end{bmatrix},$$

$$X_{180} = \begin{bmatrix} 1 & 0 & 0 & 0 \\ -0.0054 & 0.9807 & 0.0052 & -0.0137 \\ -0.0060 & 0.0023 & -0.9886 & 0.0253 \\ -0.0070 & -0.0194 & -0.0200 & -0.9862 \end{bmatrix},$$

$$Y_{180} = \begin{bmatrix} 1 & 0 & 0 & 0 \\ 0.0078 & -0.9890 & -0.0039 & -0.0300 \\ 0.0023 & -0.0034 & 0.9873 & -0.0107 \\ -0.0023 & 0.0230 & -0.0121 & -0.9830 \end{bmatrix},$$

$$\mathcal{I} = \begin{bmatrix} 1 & 0 & 0 & 0 \\ -0.0014 & 0.9784 & 0.0774 & 0.0490 \\ 0.0018 & -0.0663 & 0.9746 & -0.0709 \\ 0.0029 & -0.0587 & 0.0711 & 0.9809 \end{bmatrix}.$$

In case (ii):

$$X_{90} = \begin{bmatrix} 1 & 0 & 0 & 0 \\ -0.0001 & 0.9831 & -0.0316 & -0.0112 \\ -0.0011 & -0.0115 & 0.0323 & -0.9752 \\ -0.0025 & 0.0375 & 0.9904 & 0.0326 \end{bmatrix},$$

$$Y_{90} = \begin{bmatrix} 1 & 0 & 0 & 0 \\ -0.0001 & 0.0324 & 0.0130 & 0.9793 \\ 0.0008 & 0.0359 & 0.9875 & -0.0112 \\ 0.0009 & -0.9887 & 0.0454 & 0.0334 \end{bmatrix},$$

$$X_{180} = \begin{bmatrix} 1 & 0 & 0 & 0 \\ -0.0006 & 0.9760 & 0.0284 & -0.0132 \\ 0.0027 & 0.0242 & -0.9833 & 0.0115 \\ -0.0015 & -0.0096 & 0.0011 & -0.9907 \end{bmatrix},$$

$$Y_{180} = \begin{bmatrix} 1 & 0 & 0 & 0 \\ 0.0025 & -0.9858 & -0.0211 & -0.0139 \\ -0.0017 & -0.0248 & 0.9835 & -0.0045 \\ 0.0001 & 0.0052 & -0.0117 & -0.9853 \end{bmatrix},$$

$$\mathcal{I} = \begin{bmatrix} 1 & 0 & 0 & 0 \\ -0.0013 & 0.9703 & 0.0627 & 0.0553 \\ 0.0004 & -0.0489 & 0.9639 & -0.1045 \\ -0.0014 & -0.0662 & 0.1064 & 0.9687 \end{bmatrix}.$$

In case (iii):

$$X_{90} = \begin{bmatrix} 1 & 0 & 0 & 0 \\ -0.0022 & 0.9557 & 0.1418 & -0.1359 \\ 0.0002 & -0.1352 & -0.0813 & -0.9685 \\ 0.0061 & -0.1594 & 0.9464 & -0.0679 \end{bmatrix},$$

$$Y_{90} = \begin{bmatrix} 1 & 0 & 0 & 0 \\ 0.0029 & -0.0743 & 0.1025 & 0.9628 \\ -0.0059 & -0.1145 & 0.9502 & -0.0976 \\ 0.0024 & -0.9610 & -0.1246 & -0.0932 \end{bmatrix},$$

$$X_{180} = \begin{bmatrix} 1 & 0 & 0 & 0 \\ 0.0044 & 0.9531 & -0.0016 & 0.1211 \\ 0.0036 & -0.0126 & -0.9621 & 0.0081 \\ -0.0208 & 0.1438 & 0.0013 & -0.9624 \end{bmatrix},$$

$$Y_{180} = \begin{bmatrix} 1 & 0 & 0 & 0 \\ 0.0016 & -0.9598 & 0.0121 & -0.0085 \\ -0.0001 & 0.0083 & 0.9462 & 0.1687 \\ -0.0027 & -0.0234 & 0.1564 & -0.9575 \end{bmatrix},$$

$$\mathcal{I} = \begin{bmatrix} 1 & 0 & 0 & 0 \\ -0.0044 & 0.9029 & -0.0594 & -0.0698 \\ -0.0002 & -0.0180 & 0.9424 & 0.0190 \\ -0.0183 & 0.0563 & -0.0120 & 0.9083 \end{bmatrix}.$$

### Design of Benchmarking sequences and Simulation Using Lindblad Equation

We generated 150 random sequences for each length of Clifford gates for the RB and PB experiments, up to 55 Clifford gates. Each sequence had randomly selected Clifford gates such that the Clifford group was sampled uniformly. For the experiment, we only used Clifford gate sequences of length  $m=1, \dots, 7, 9, 11, 16, 19, 23, 28, 30, 33, 36, 39, 40, 44, 45, 48, 49, 53, 55$  for the RB without SEL; length  $m=1, \dots, 7, 9, 14, 17, 20, 22, 25, 27, 31, 35, 37, 40, 41, 42, 45, 49, 54, 55$  for the PB without SEL; length  $m=1, \dots, 7, 10, 13, 14, 16, 17, 21, 23, 26, 27, 31, 33, 37, 41, 43, 45$  for the RB with SEL; length  $m=1, \dots, 8, 9, 13, 17, 18, 19, 22, 27, 29, 32, 34, 38, 40, 43, 47$  for the PB with SEL. Longer sequences could not be sampled mainly due to the limitation of the TWT amplifier.

We also numerically simulate our benchmarking experiments. The simulation evolves an initial density matrix according to the Lindblad model using the same pulse sequences as in the experiments. Experimentally measured  $T_1=160 \mu\text{s}$  and  $T_2=30 \mu\text{s}$  are used in the simulation. We incorporate the effects of  $T_2^*$  and local  $B_1$  field inhomogeneities by averaging the simulation over these distributions (see Fig. 8 for the Larmor frequency distribution, which corresponds to the  $T_2^*$  effect, and see Fig. 9 for the local  $B_1$  distribution). The SEL sequence is used in the experiments to effectively extend  $T_{2,\text{no SEL}}^* \sim 80$  ns. This sequence is comprised of eight  $2\pi$  rotation pulses, each separated by an order of  $T_2$  to allow the transverse components to dephase [34]. This SEL sequence selects a subset of the spin ensemble within narrower Larmor frequency distribution while dephasing most of the off-resonance spin packets as shown in Fig. 8, but we found that it does not have much effect on the  $B_1$  distribution. The SEL step is incorporated in the simulation by using a distribution that matches the Larmor frequency distribution measured in the experiments with SEL sequences ( $T_{2,\text{SEL}}^* \sim 160$  ns).

Figures 12 and 13 show the simulation results of RB and PB protocols when taking and not taking SEL sequences into account. These simulations only take into account  $T_2^*$  distribution since we simulated that our measured  $B_1$  field inhomogeneity has little effect on our BEPG ( $< 10^{-4}$ ). The values from the simulation with no SEL sequences are  $\epsilon = 0.0049(1)$  and  $\epsilon_{\text{in}} = 0.0046(1)$ . The values from the simulation using the Larmor frequency distribution with SEL sequences are  $\epsilon = 0.0040(0)$  and  $\epsilon_{\text{in}} = 0.0035(0)$ . As simulations assume no pulse distortions (*i.e.*, perfect knowledge of  $\mathcal{T}$ ), the only coherent error source in the simulations is the imperfection in the OC pulse design which is very small (see Table III).

In the case with short  $T_2^*$ , the simulated decays slightly deviate from a single exponential decay, while the simulated decays in the case with long  $T_2^*$  can be fitted very well to a single exponential decay up to  $\sim 50$  gates, which agrees with the experimental results. This indicates the  $T_2^*$  effect contributes to the non-Markovian noise.

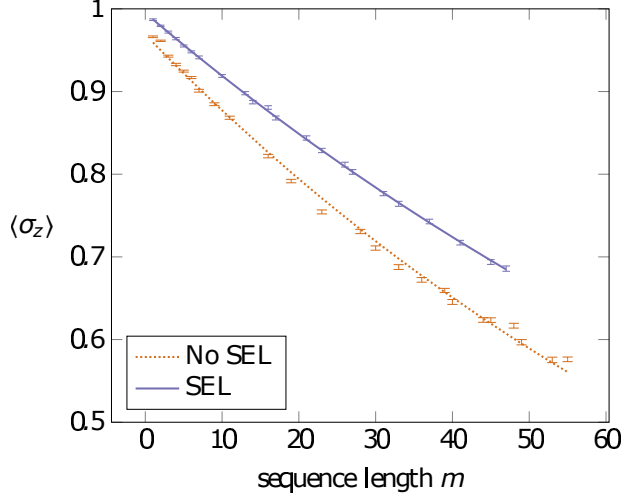


Figure 12. (Color online) Simulation results of RB using the same pulse sequences as in the experiments. ‘SEL’ and ‘No SEL’ denote the cases of  $T_2^* \sim 160$  ns and  $T_2^* \sim 80$  ns, respectively. The solid and dotted lines are least squares fits to  $B(1 - 2\epsilon)^m$  where  $\epsilon$  is the BEPG for the Clifford group. The error bars indicate the standard error of the mean.

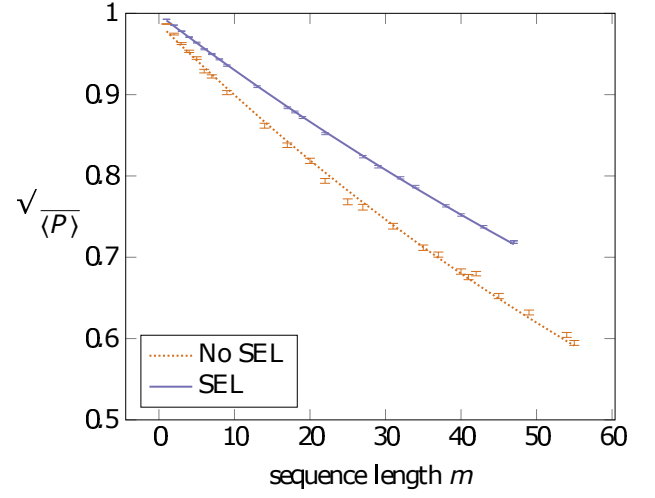


Figure 13. (Color online) Simulation results of PB using the same pulse sequences as in the experiments. ‘SEL’ and ‘No SEL’ denote the cases of  $T_2^* \sim 160$  ns and  $T_2^* \sim 80$  ns, respectively. The solid and dotted lines are least squares fits to  $\sqrt{B'(1 - 2\epsilon_{\text{in}})^{(m-1)}}$  where  $\epsilon_{\text{in}}$  is the IEPG for the Clifford group. The error bars indicate the standard error of the mean.